THE JOURNAL OF PHYSICAL CHEMISTRY B

ARTICLE

pubs.acs.org/JPCB

Conformation, Defects, and Dynamics of a Discotic Liquid Crystal and Their Influence on Charge Transport

Lucas A. Haverkate,[†] Mohamed Zbiri,[‡] Mark R. Johnson,[‡] Bruno Deme,[‡] Fokko M. Mulder,*[,†] and Gordon J. Kearley[§]

[†]RID, Faculty of Applied Sciences, Delft University of Technology, Mekelweg 15, 2629JB Delft, The Netherlands

[‡]Institut Laue Langevin, 38042 Grenoble Cedex 9, France

[§]Bragg Institute, Australian Nuclear Science and Technology Organisation, Menai, NSW 2234, Australia

Supporting Information

ABSTRACT: Future applications of discotic liquid crystals (DLCs) in electronic devices depend on a marked improvement of their conductivity properties. We present a study of 2,3,6,7,10,11-hexakishexyloxytriphenylene (HAT6) and show how local conformation, structural defects, and thermal motions on the picosecond time scale strongly affect the efficient charge transport in DLCs. A direct and successful comparison of classical molecular dynamics (MD) simulations with both neutron powder diffraction and quasielastic neutron scattering (QENS) give a full insight into the structural and dynamical properties of HAT6. The local conformation of HAT6 molecules is characterized by a mutual rotation (twist) angle of about 37° and *typically* a mutual aromatic-core distance of 3.4 Å instead of the average distance of 3.65 Å usually quoted. We show that a considerable number of structural traps is present in HAT6, which persist at the picosecond time scale. We find that the high disorder in the mutual positions of the aromatic cores is an important factor contributing to the limited conductivity of HAT6 compared to larger DLCs.

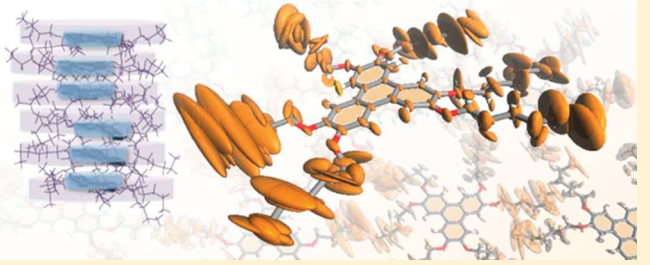

INTRODUCTION

Discotic liquid crystals (DLCs) are a promising class of materials for molecular electronic devices.[1−3] They have low cost, are relatively easy to process, and show molecular self-organization. In the liquid crystalline phase, the disk-like molecules stack on top of one another into stable columns due to the overlap of the π-orbitals of their aromatic core, while thermal fluctuations of the side chains give rise to the liquid-like dynamic disorder. The stacks of aromatic cores provide a one-dimensional pathway for charge-carrier transport along the column direction, in most cases with the holes as major charge carriers.[4−6] This makes discotics promising candidates for application in organic devices such as light emitting diodes, field-effect transistors, and photovoltaic cells.[7−9]

However, efficient charge transport in DLCs strongly depends on three main factors. First, the local molecular arrangement should be optimal. Since charge transport in discotics is described by the hopping formalism according to Marcus theory,[6,10,11] the charge transfer between neighboring molecules within a column strongly depends on their relative positions and orientations. The probability for charge hopping would be maximal when the intermolecular separation is minimal, with the polyaromatic cores being on top of each other (no lateral slide) and the mutual orientation being cofacial.[6,12−14] Second, the number of structural defects must be minimal on a large spatial scale, since one-dimensional charge transport is limited by the slowest transfer rates.[13,15] Finally, the thermal motion of the molecules perturbs the rather "soft" charge-transport system. Charge transfer between neighboring molecules, which is on the picosecond time scale,[16,17] is hindered by the slow whole-body movements of the discs on similar and slower time scales.[6,18]

Recent work on hexabenzocoronene (HBC) derivatives[15,19−24] and semitriangle-shaped discotic molecules[13,25] showed that classical molecular-dynamics (MD) simulations are of key importance in determining the influence of structure and dynamics on the conductivity of DLCs. MD simulations are capable of predicting the conductivity of the mesophases and reveal how local conformation, disorder, and dynamics affect efficient charge transfer along the 1D column pathway. However, to realize the possibility for rational design of compounds with optimal structure−mobility relationships, it is necessary to verify that the MD simulations describe the real liquid-crystalline phase correctly. Although the DLC structures from MD simulations were successfully compared to experiments on lattice constants, density, phase-transition temperatures, order parameter, and mutual orientation (twist angle) in specific cases, a more thorough analysis such as Rietveld refinement on crystalline structures was not performed.

In this work, we make the first full comparison between experiments and both the structure and dynamics of a discotic

Received: July 18, 2011
Revised: September 22, 2011
Published: October 06, 2011

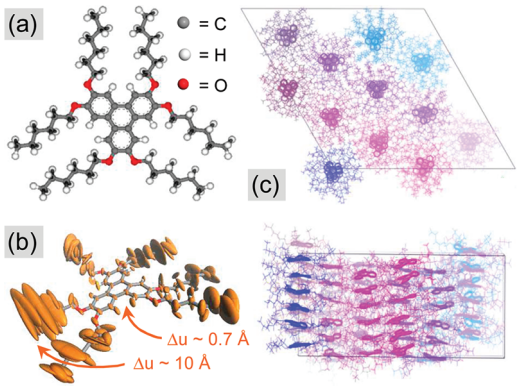

Figure 1. (a) HAT6 in its D_{3h} symmetric configuration, (b) anisotropic temperature factors for a HAT6 molecule with atomic displacements ranging from 0.7 Å (aromatic core) to 10 Å (tail end), and (c) MD simulation snapshot of TWIST25.

liquid crystal as predicted by MD simulations. As a model system, we use the typical discotic liquid crystal 2,3,6,7,10,11-hexakishexy loxytriphenylene (HAT6); see Figure 1a. HAT6 is a member of the widely discussed HAT*n* series,[6,11,12,14,18,26−31] but it is still an open question how its limited charge carrier mobility of about 10^{-4} cm^2 V^{-1} s^{-1} as measured with PR-TRMC[16] relates to the much better mobilities in larger molecules such as HBC C-12.[5,20] By comparing classical MD simulations with neutron powder diffraction, a previous quasi-elastic neutron scattering (QENS) experiment,[18] and first-principles DFT calculations,[28] we not only identify the local molecular conformation, structural defects, and thermal motions in HAT6 but also discuss their effect on charge transport in relation to HBC-C12. We find a counter-intuitive difference between the typical distance between aromatic cores and the average molecular separation within a column, which is of key importance for good conductivity in DLCs.

MATERIALS AND METHODS

Sample Preparation. Isotopically normal 2,3,6,7,10,11-hexakishexyloxytriphenylene (HAT6) and its side-chain deuterated analogue, HAT6D, were prepared by the synthesis methods described earlier.[32,33] The deuteration of HAT6D was 98 atom %.

Neutron Powder Diffraction. Neutron powder diffraction on HAT6 and HAT6D was performed using the D16 diffractometer at the Institut Laue Langevin (ILL) in France. We selected a wavelength of 4.54 Å to get a good compromise between *d*-spacing range and angular resolution. The diffraction patterns of HAT6 and HAT6D were obtained for the columnar liquid-crystalline phase at 345 K, after heating the samples from the room-temperature crystalline state. The advantage of using neutron diffraction over X-ray diffraction is that elements with a small number of electrons have a small X-ray scattering cross section, while the neutron scattering cross section is determined by the nucleus and is relatively large in the case of deuterium. As a consequence, the neutron powder diffraction pattern of the tail-deuterated sample HAT6D provides more information about the crystal structure than earlier[30,34] X-ray powder diffraction experiments.

Quasielastic Neutron Scattering. We determined the dynamics on the picosecond time scale by directly comparing the quasielastic neutron scattering (QENS) spectra of the two MD simulation models TWIST25 and TWIST60 with experiments. QENS has the advantage that neutrons follow both the temporal and spatial characteristics of atomic motion via a well-characterized interaction with the atomic nuclei. Consequently, it is fairly straightforward to calculate the expected spectral profiles by using the atomic trajectories from the MD simulations. If these are in acceptable agreement with the observed spectra, we cannot only validate the typical time scales of motion but also assign them to the underlying mechanisms. Further details about the experiment and the theoretical basis can be found elsewhere.[18] The incoherent scattering functions of the MD trajectories were calculated using the nMOLDYN suite[35] with a resolution of 0.05 meV, this being similar to the experimental conditions.

Molecular Dynamics Simulations. For large molecular systems such as that discussed here, force-field methods are considered to be the best alternative to the more accurate quantum-mechanical approaches that are computationally too expensive in the present case. In practice, force-field methods enable accurate and simultaneous predictions of structural, conformational, vibrational, and thermo-physical properties, not because the systems considered behave mechanically but because force fields are adjusted to reproduce relevant observables and therefore include many effects empirically. An important aspect in the case of stacked aromatic aggregates is a proper description of the dominant $\pi-\pi$ interaction between the aromatic rings. The main term in this interaction is the London dispersion energy[36−41] and force fields are capable of reliably describing $\pi-\pi$ interactions via the Lennard-Jones function, although improvements could be made by including recent developments.[37,39,40] The force field employed in this work is the COMPASS module[42−44] in the Materials Studio suite. COMPASS is a second-generation force field, which generally achieves higher accuracy by including cross terms in the energy expression[42] to account for such factors as bond, angle, or torsion distortions caused by nearby atoms. The force field parameters as well as a thorough validation of COMPASS for poly ethylene oxide, alkene, and benzene compounds can be found elsewhere.[42,44]

The Model Systems. To obtain a reliable description of the liquid-crystalline phase, large model systems are necessary ensuring that a sufficient part of the structural disorder is incorporated. A common method to reduce the computational effort involved is to use a united atom approach for the side chains of discotics, allowing system sizes of more than 200 molecules.[13,22] However, in the present study, an *all-atom* force field was necessary in order to compare the MD simulations directly with neutron powder diffraction patterns and QENS experiments. We considered a periodic hexagonal supercell consisting of 72 HAT6D molecules (10368 interacting atoms), a much larger system than other *all-atom* models carried out for discotics.[18] Earlier MD calculations on HAT5 with a comparable system size (but using a united atom approach) already showed that such a size is sufficient to incorporate the essential properties of the liquid crystalline phase.[31] We arranged the 72 molecules in 12 columns, each column consisting of 6 molecules. Initial sizes of 72.9 and 21.9 Å were selected for the *a*-axis and *c*-axis of the supercell, respectively, corresponding to a column−column distance of 21.04 Å between molecules in different columns, and a nearest-neighbor disk−disk spacing of 3.65 Å within a column. These values concur with the observed reflections in the neutron powder diffraction pattern and agree well with the measured density of 0.97 ± 0.04 g cm^{-3} for HAT6. The initial molecular conformation of the HAT6 molecules is shown in Figure 1a.

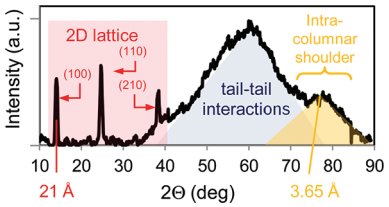

Figure 2. Neutron diffraction pattern of HAT6D at 345 K, with the 2D lattice of columns (red) and distributions in tail−tail (blue) and intracolumn (yellow) distances.

It has been preoptimized using COMPASS, with a fixed D_{3h} molecular symmetry, the tail torsions being all-trans.

To inspect the dependence of the results on starting configuration, two models were tested considering the mutual rotation of the molecules. In the first model TWIST60, the nearest-neighbor molecules in a column are rotated by 60° around their principal axis, while molecules in one 2D layer have a similar orientation. In the second model, TWIST25, we have built a unit of three columns by taking a twist angle of 25° for the first column, then taking the same mutual rotation angle but in the opposite direction for the second column, and finally constraining the twist angle of the third column to 5° in order to avoid superposition of the tails.

The final MD simulations were obtained after a few preparation steps. First, the initial models were geometrically relaxed with the same nonbond settings in COMPASS as used for the MDs. Then, a sequence of (NPT) MD runs was performed for thorough relaxation and equilibration of the systems. The total time of the sequence was 2 ns for both models. Final MD production runs of 500 and 750 ps were executed for TWIST60 and TWIST25, respectively. We checked that the prerelaxation sequence was sufficient to bring the system in equilibrium: a longer run of 3 ns did not change the monitored properties significantly. As a reference, we also performed a 750 ps run on a prerelaxed isolated molecule. From these simulations, all data necessary for calculating structural and dynamical properties was extracted using Materials Studio scripts.

Technical Details. To mimic the experimental conditions under which the neutron powder diffraction patterns and QENS spectra were obtained, the system was held at a pressure of 0.1 MPa and a temperature of 345 K (NPT ensemble) using Berendsen's method.[45] The coupling to the external bath was established with both the pressure and temperature relaxation time set at 1 ps. For the MD simulations, a time step of 1 fs was chosen; longer time steps normally lead to unreliable results, since the vibration of the hydrogen atoms is in the order of femtoseconds. The Coulomb and van der Waals interactions were summed using the atomistic approach,[46] the Lennard-Jones function being truncated at a cutoff distance of 10 Å. A spline wdth of 1.3 Å was chosen in order to turn off the nonbond interactions smoothly. A long-range correction for the effects of splining and cutoff was applied in the standard way.[47] The cut-off value of 10 Å is less than half the size of the shortest axis of the supercell (21 Å), while being large enough (in combination with the long-range correction) for a sufficient incorporation of the long-range nonbond interactions.[46,47] The atomic charges were assigned using the COMPASS force field.

Simulated Powder Diffraction Patterns. A crucial step in our approach is a direct comparison of the experimental neutron powder diffraction pattern with a crystal structure extracted from the MD simulations. The Reflex package in Materials Studio is capable of calculating and refining the diffraction pattern of crystal structures with more than 500 atoms in a unit cell. To make the comparison as direct as possible, only the instrumental zero-point offset was refined.

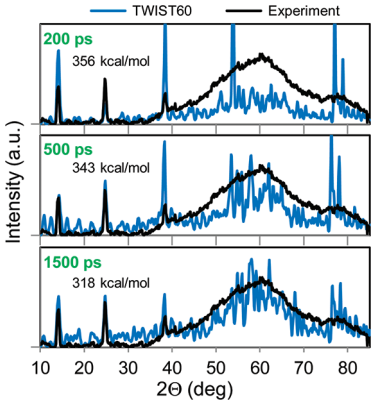

Figure 3. Comparison of the simulated diffraction pattern of TWIST60 with the experimental pattern. The potential energy and diffraction pattern were calculated after 200, 500, and 1500 ps.

RESULTS

Figure 1c illustrates a typical snapshot of the MD simulations, showing the hexagonal packing of HAT6 into stable columns. Details of the thermodynamic properties of the simulations can be found in the Supporting Information.

Comparison of MD Simulations with Neutron Diffraction. In the columnar phase, the diffraction pattern of a discotic liquid crystal can be conveniently subdivided into three regions. For the neutron diffraction pattern of HAT6D, this is illustrated in Figure 2. The red area indicates a region with three sharp peaks originating from the 2D hexagonal lattice, the (100) peak corresponding to an average column−column distance of 21 Å. The blue region originates from the broad distribution in tail−tail distances, with a maximum at 4.5 Å. The intracolumnar distances correspond to the broad yellow shoulder around 3.65 Å. The tail−tail region and shoulder disappear almost completely for the fully protonated sample. Thus, the shoulder represents intracolumnar distances between whole molecules rather than only the core−core separation.

The crystal structure predicted by the MD simulations should reproduce the three regions in the diffraction pattern in order to be sure that a proper minimum is found in the large configuration space. To determine this, we first followed the evolution of the neutron diffraction pattern during the MD relaxation procedure. Figure 3 shows the calculated diffraction patterns of the intermediate structures after 200, 500, and 1500 ps for the MD relaxation of the initial model TWIST60 (TWIST25 gives comparable results). Clearly, the simulated structure converges toward the experimentally observed phase during the MD relaxation, while the free energy of the crystal decreases to its minimum. The high mismatch of the 2D lattice peaks after 200 ps indicates that the initial TWIST60 model, with a twist angle of 60°, is far from the equilibrium liquid-crystalline phase. The improved reproduction of the tail−tail and intracolumnar region during the relaxation process reflects the distribution of the tail dihedral angles and core−core spacing during the MD relaxation.

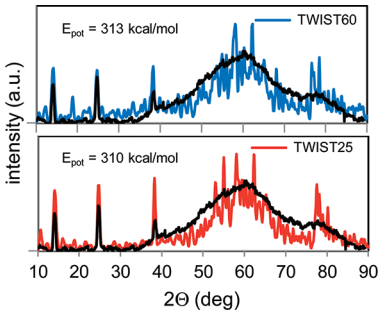

Figure 4. Diffraction patterns of TWIST60 and TWIST25 compared with experiment (black line), calculated from the average structure and temperature factors using 500 ps of the final MD runs.

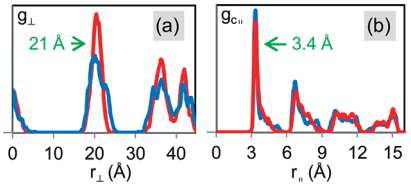

Figure 5. Positional correlation functions of the aromatic cores (a) perpendicular to the column axis and (b) parallel intracolumnar, for both TWIST25 (red) and TWIST60 (blue).

As a second step, we included the dynamical behavior of the liquid-crystalline phase in the comparison of the MD simulations with the experimental observations. We extracted the average structure and deviations from this by using 500 ps of the final MD runs on TWIST25 and TWIST60. The dynamic behavior was included by calculating the anisotropic temperature factors corresponding to the atomic displacements (Figure 1b). The tail atoms show large displacements of about 10 Å.

Figure 4 shows the calculated diffraction patterns corresponding to these thermally averaged structures. For the TWIST60 model, the time-averaged diffraction pattern strongly resembles the snapshot after 1.5 ns MD relaxation, showing that the prerelaxation sequence was sufficient to bring the system in equilibrium. The main difference between TWIST25 and TWIST60 is the higher intensity of the 2D hexagonal lattice peaks for TWIST25. This indicates that the liquid-crystalline phase obtained with the initial TWIST25 configuration is more ordered than the final TWIST60 structure, which is indeed the case as will be shown in the next sections. The experimentally observed diffraction pattern is intermediate between the simulated patterns of the models. On the one hand, TWIST25 shows too high peak intensities for the 2D hexagonal lattice and a couple of peaks in the tail−tail region. On the other hand, for TWIST60, the background in the 2D lattice region is higher than observed experimentally, indicating an overestimation of the 2D disorder. Furthermore, the order in intracolumnar distances and the intensity of the (210) peak is overestimated in both cases. Despite these differences, both the diffraction pattern of TWIST60 and TWIST25 show remarkable agreement with the experimental pattern, while the relaxed structures stem from entirely different starting configurations. In the next sections, the structural similarities and differences between the two models will be discussed. Here, we already anticipate that both models converge to comparable minima in configuration space, close to the actual

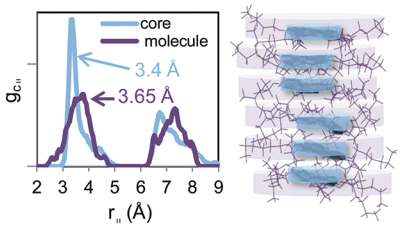

Figure 6. Parallel intracolumnar correlation functions of the molecules and only the aromatic cores, extracted from TWIST25. The right figure is a snapshot, illustrating the difference between the distribution of core−core and molecular separation.

liquid-crystalline structure considering the agreement with the experimental diffraction pattern.

Structural Properties of the Liquid-Crystalline Phase. The liquid-crystalline structure of discotics is characterized by orientational order, positional order, twist-angle distribution, and the distributions in tail dihedral angles. Here, we focus on positional order and twist-angle distribution; for the orientational order and tail dihedral angles, see the Supporting Information.

Positional Order. We determined the order between and within the columns by calculating the positional correlation functions of HAT6 cores perpendicular and parallel to the column director.[31] Figure 5 shows these correlation functions for 500 ps of the final MD runs on TWIST25 and TWIST60. The core positions were estimated by calculating the center-of-mass (CM) of the aromatic cores. The perpendicular correlation function, $g_{\perp}$, reflects the order in the 2D lattice of columns, with a nearest column distance of 21 Å and additional peaks at 36.4 and 42 Å due to the hexagonal arrangement. The width of the nearest-column peak is 6.0 Å for TWIST25 and 9.0 Å for TWIST60, indicating that the TWIST25 configuration is more ordered considering the 2D hexagonal arrangement of molecules. In the TWIST60 configuration, some molecules are laterally shifted with respect to the average column position. These defects give rise to the shoulder in the nearest-column peak appearing around 23.5 Å and explain the less intense 2D lattice peaks in the diffraction pattern. Considering both models, we can conclude that a significant fraction of the molecules shows a deviation with respect to the column axis, with a corresponding lateral slide of 2.5 Å, or even higher. The parallel separations between the aromatic cores within a column are represented by the parallel intracolumnar correlation function, $g_{\parallel}$, in Figure 5b. Contrary to the perpendicular correlation, there is no significant difference in parallel intracolumnar correlation between TWIST60 and TWIST25. Interestingly, the corresponding distribution of core−core distances (cofacial distances separating the planes of the aromatic cores) is in both cases highly asymmetric, with a narrow peak at 3.4 Å and a broad tail extending in excess of 5 Å. The *typical* core−core distance of 3.4 Å agrees with the observed distance between HAT1 molecules.[48] On the other hand, the distribution in the cofacial distances between the *molecular* planes is almost symmetric around 3.65 Å for both models (Figure 6), in line with the experimentally observed intracolumnar shoulder which is dominated by diffraction from the deuterated tails. The molecular positions were determined from the center of mass of the HAT6 molecules, including the tails.

These observations indicate that the competition between the mutual van der Waals interactions of the cores with the steric repulsion of the tails causes a high disorder in the core−core distances rather than a uniform shift of the core−core distance

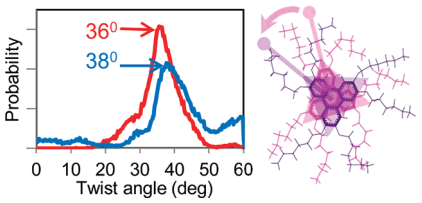

Figure 7. Twist-angle distribution for TWIST25 (red) and TWIST60 (blue).

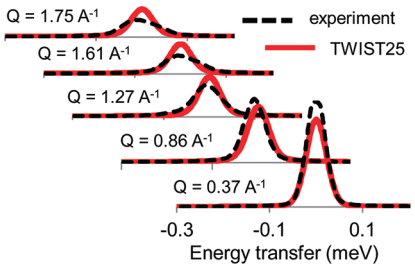

Figure 8. Comparison of the incoherent scattering function from the simulation TWIST25 with the measured function at 348 K.

distribution to higher distances. The tails tend to orient toward the open spaces formed by these core−core defects, since the whole-molecule peak lies at a higher distance than the core−core peak. For both TWIST25 and TWIST60, all the core−core distances are larger than 3 Å, about 35% are larger than 3.7 Å, and about 20% are larger than 4 Å. The dimers with a core−core distance larger than 4 Å can be considered as structural traps on the picosecond time scale; see the Supporting Information. On the basis of the comparison with neutron diffraction (Figure 4), even this disorder in intermolecular and core−core distances along the column direction seems slightly underestimated, likely due to the limited size of the models in the columnar direction.

Twist-Angle Distribution. The twist angle of two HAT6 molecules is defined as the mutual rotation angle of their molecular planes (Figure 7). We used the vectors between the center of the core and the oxygen atoms to extract the twist angles from the models. Figure 7 shows the twist-angle distribution between the nearest-neighbor molecules within a column. The twist-angle distribution peaks are around 36 and 38° for TWIST25 and TWIST60, respectively. These values are in good agreement, especially taking into account that the equilibrated structures stem from entirely different initial models. Moreover, they are comparable to the typical twist angle for HAT5 derived from molecular dynamics[31] and close to the minimum-energy twist angle of 30° as calculated with DFT.[28] The initial TWIST25 configuration with two columns set at 25° is closer to the equilibrium twist angle, which results in a sharper distribution. The TWIST60 distribution is broader, with a small additional peak at 60° originating from about 17% of the molecules that were not able to rotate during the relaxation. However, also TWIST25 shows these twist-angle defects: about 3% of the molecules have a twist angle larger than 50°. Interestingly, this disorder in the twist-angle distribution is coupled to the disorder in the 2D lattice of columns discussed earlier. The molecules with positions shifted with respect to their columns often show significant deviation from the equilibrium twist angle, resulting in a correlation coefficient of about 0.5 for the linear dependence between lateral slide and

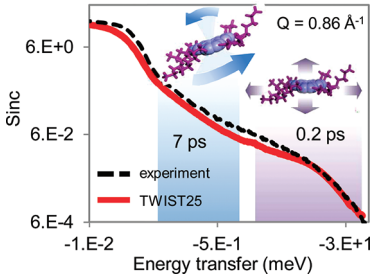

Figure 9. Incoherent scattering function at ~345K and $Q = 0.86$ A^{-1} on a log scale for both experiment and TWIST25 simulation. The colored areas indicate the regions of dominant rotational (7 ps) and translational (0.2 ps) motion. The elastic region is emphasized by the gray area.

twist angle. These structural defects with a coupled deviation in twist angle and lateral slide explain the smaller intensities of the 2D hexagonal-lattice peaks in the neutron diffraction pattern of TWIST60: the equilibrated TWIST60 structure is more disordered than TWIST25 in both twist-angle distribution and lateral slide.

Dynamic Behavior on the Picosecond Time Scale. To characterize the dynamical processes on the picosecond time scale, we compared our MD simulations with earlier QENS experiments. In the analyses of the experiments, it was consistently found that in addition to the elastic peak at least two Lorentzian functions are required to fit the data. The fwhm peak widths corresponded to time scales of about 0.2 and 7 ps. Figures 8 and 9 show the incoherent-scattering function extracted from the TWIST25 simulation together with the measured function at 348 K. The agreement is satisfactory, and it is certain that a proper rescaling of the simulation temperature[18] or using larger simulation models could give even better agreement. The moderate size of the models could explain that the width of the simulated scattering function increases slower with Q than the experimental signal. The long-range molecular motions are very likely suppressed in the simulation, leading to a more "stiff" response compared to the actual liquid-crystalline phase. However, the essential observation is that the TWIST25 and TWIST60 models compare well with the measured temporal and spatial dynamics (Figure 9). For both models, the intensities and time scales of the two spectral components are in reasonable agreement with experiment.

The agreement with experiment allows us to identify the underlying thermal motions by examining the simulation trajectories more closely. We estimated the typical amplitudes of molecular motion on the 0.2 and 7 ps time scale by extracting the translational (parallel and perpendicular to the column axis) and rotational (tilt and twist) movements of several molecules. Figure 10 illustrates the characteristic translational and tilt motions for a single molecule on the 0.2 ps time scale. The twist-angle deviations are negligible on this time scale with amplitudes smaller than 0.1°. Apparently, the tilt movement of the molecular core is too fast to be followed by the aliphatic tails: the tilt angle of the whole molecule hardly shows any changes on this time scale, while the tilt motion of the core has an amplitude of about 1.5°. The latter corresponds to displacements of the core hydrogen atoms of about 0.1 Å. In contrast, the core and tail dynamics of translations are correlated, with typical amplitudes of about 0.1 and 0.15 Å for ~0.2 ps motions perpendicular and

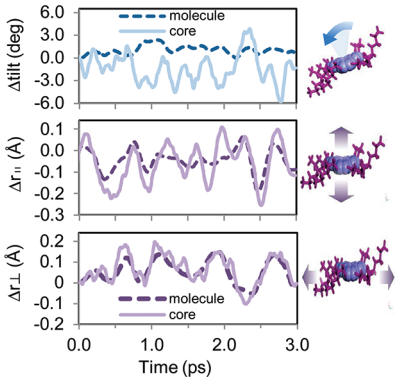

Figure 10. Subpicosecond translational and tilting motion for a typical molecule extracted from the TWIST25 trajectory, for both the molecular center of mass (CM) including the tails (broken lines) and the movement of the aromatic core CM alone.

parallel to the column axis, respectively. The tails completely follow the perpendicular (lateral) motion of the aromatic core, while their correlation with the parallel motion of the core is weaker. On the 7 ps time scale, the rotational motions are much more prominent: the aliphatic tails start to "follow" the rotations of the core (Supporting Information, Figure S3), with amplitudes of about 0.7 and 1.5° for tilt and twist motions of the whole molecule. The corresponding displacements of the tail hydrogens are between 0.1 and 0.3 Å, stronger than the translational displacements on the 7 ps time scale.

From the above observations, we conclude that molecular translations ("in-plane" motions) make the dominant contribution to the spectral component of 0.2 ps in the QENS spectrum, while the 7 ps component mainly stems from both tilt and twist motion of the whole molecule (Figure 9). This is a slightly different assignment than the one obtained for an MD simulation on a single column of four molecules, with the 7 ps component only attributed to the tilt ("out-of-plane") motions.[18] The difference probably arises from the more constrained twist motion of the HAT6 molecules in the presence of the neighboring columns, the present models being a more realistic representation of both structure and dynamics of the liquid crystalline phase than was possible previously.

DISCUSSION

The mobility of HAT6 (10^{-4} cm^2 V^{-1} s^{-1}) for charge transport along the column director is about 3 orders of magnitude smaller than larger DLCs such as HBC-C12 (0.4 cm^2 V^{-1} s^{-1} measured with PR-TRMC).[5,11,24] What are the main factors contributing to this difference?

According to the Marcus formalism, the electron (hole) transfer rate ω_{ij} from two identical molecules i and j in the absence of an external field is described by[10,13]

$$\omega_{ij} = \frac{|J_{ij}|^2}{\hbar}\sqrt{\frac{\pi}{\lambda kT}}\exp\left[-\frac{\lambda}{4kT}\right]$$

This equation provides two key parameters governing charge transport in disordered materials: the reorganization energy λ and the charge transfer integral J_{ij}. For (small) DLCs, the reorganization energy is dominated by the internal molecular contribution, which is 0.1 eV for HBC and 0.18 eV for triphenylene.[15] As a first estimation, the reorganization energy therefore accounts for about 1 order of magnitude smaller transfer rate for HAT6 compared to HBC-C12. The charge transfer integral, on the other hand, is very sensitive to the relative molecular arrangement.[6,15] Knowledge about the parametric dependence of J on relative positions and orientations can be very helpful for optimizing the charge-carrier mobility of DLCs, for instance, in realizing the optimal register of twist angles, as has been recently achieved by Feng et al. for triangle-shaped molecules.[13] For HAT6, the twist angle of 37° we found will reduce J to about 50% compared to the optimal angle of 0°, as estimated from previous DFT calculations.[28] However, this *typical* twist angle does not account for a lower mobility of HAT6 compared to HBC-C12. The twist angle of about 30° found for HBC-C12[22] even leads to a smaller value of the transfer integral in comparison with HAT6 at 37° at a similar core−core separation.[6] However, the overall mobility is not only sensitive to the standard order parameters, such as the typical twist angle and the orientational order parameter. Instead, it is the whole *distribution* of molecular positions and orientations that influences the overall charge transport along the column. Charge transport is in particular dominated by the tail of the distribution showing the lowest $|J|^2$ values, since for one-dimensional transport the mobility is limited by the slowest rates. This makes the mobility very sensitive to the presence of structural defects and allows us to estimate their effect on the charge transport by focusing on the molecular couples having the lowest transfer integral.

Considering the disorder in molecular separations along the column director, we found for HAT6 that about 20% of the aromatic cores are mutually separated with more than 4 Å, with a tail extending in excess of 5 Å. They act as structural traps for charge transport, as discussed in the Supporting Information. For HBC-C12, the disorder in intracolumnar distances is much less pronounced, with a maximum molecular separation below 4 Å.[22,23] The charge-transfer integral decreases exponentially as a function of core−core distance,[13,14,28] approximately as $J \sim \exp(-2.2z/\text{Å})$ for both HBC and triphenylene.[13,15] Taking into account that the aromatic core dominates the transfer integral,[6,28] a separation of 5 Å for HAT6 molecules then leads to about 2 orders of magnitude smaller $|J|^2$ than HBC-C12 molecules with a mutual distance of 4 Å. Such a large difference, although being a first approximation, clearly indicates that the structural disorder in core−core distances found for HAT6 is a major factor limiting charge transport compared to HBC-C12.

Considering the disorder in twist angle, we found that at least 3% of the HAT6 dimers show twist angles larger than 50°, a situation leading to very small transfer integrals if the molecules are not laterally translated.[28] However, the disorder in twist angle appeared to be correlated to the disorder in lateral slide, making the parametric dependence on J more complicated.[6] Also, the effect of thermal motions on the mobility is not easily quantified, since the picosecond time scales of motion strongly interfere with the charge transfer between molecules that is on a similar time scale.[24,24] On the basis of the small amplitudes (Figure 10 and Supporting Information, Figure S3) of motion, it is at least reasonable to expect that their influence on charge transport is smaller than the discussed structural traps in core−core distances. Anyway, a complete and accurate analysis of the morphology−mobility relationship would require a full calculation of the distribution in transfer integrals induced by the whole time dependent register of molecular positions and orientations. The estimations presented here, however, lead to the conclusion that,

next to the difference in reorganization energy, the extremes in the disorder in core−core distances are a major factor limiting charge transport in liquid crystalline HAT6 compared to larger discotics such as HBC-C12. Suppressing these less abundant defects would be one of the most challenging steps toward the design of relatively small DLCs with optimal carrier mobilities. It is a matter of trying to change one of the most basic properties of the liquid crystalline phase.

CONCLUSIONS

We have determined the structure and dynamics of HAT6 by making a comparison of neutron diffraction and QENS data with classical MD simulations. To the best of our knowledge, this is the first time that the structure of a discotic liquid crystal has been determined by a full reproduction of its diffraction pattern. This enabled us to verify that classical MD simulations are capable of reproducing the liquid-crystalline phase accurately, which opens the possibility for rational design of compounds with optimal properties. We showed that for HAT6 the distribution in mutual aromatic-core distances in a column is highly asymmetric, with a *typical* core−core distance of 3.4 Å instead of the average distance of 3.65 Å usually quoted, with the tail of the distribution extending beyond 5 Å. This disorder in core−core distances is static on the time scale of charge transport, and it forms a main factor contributing to the limited conductivity of HAT6 compared to larger DLCs such as HBC-C12.

ASSOCIATED CONTENT

Supporting Information. Thermodynamic properties and additional properties of liquid crystalline HAT6 extracted from the MD simulations. This material is available free of charge via the Internet at http://pubs.acs.org.

AUTHOR INFORMATION

Corresponding Author
*E-mail: F.M.Mulder@tudelft.nl.

ACKNOWLEDGMENT

This work is part of the research program of the Foundation for Fundamental Research on Matter (FOM), which is financially supported by The Netherlands Organization for Scientific Research (NWO). This article is the result of joint research in the Delft Research Centre for Sustainable Energy and the 3TU Centre for Sustainable Energy Technologies.

REFERENCES

(1) Schmidt-Mende, L.; Fechtenkotter, A.; Mullen, K.; Moons, E.; Friend, R. H.; MacKenzie, J. D. *Science* **2001**, *293*, 1119–1122.
(2) Kato, T.; Yasuda, T.; Kamikawa, Y.; Yoshio, M. *Chem. Commun.* **2009**, *7*, 729–739.
(3) Kato, T.; Mizoshita, N.; Kishimoto, K. *Angew. Chem., Int. Ed.* **2006**, *45*, 38–68.
(4) Adam, D.; Schuhmacher, P.; Simmerer, J.; Haussling, L.; Siemensmeyer, K.; Etzbach, K. H.; Ringsdorf, H.; Haarer, D. *Nature* **1994**, *371*, 141–143.
(5) Van de Craats, A. M.; Warman, J. M.; Fechtenkotter, A.; Brand, J. D.; Harbison, M. A.; Mullen, K. *Adv. Mater.* **1999**, *11*, 1469–1472.
(6) Lemaur, V.; Da Silva Filho, D. A.; Coropceanu, V.; Lehmann, M.; Geerts, Y.; Piris, J.; Debije, M. G.; Van de Craats, A. M.; Senthilkumar, K.; Siebbeles, L. D. A.; et al. *J. Am. Chem. Soc.* **2004**, *126*, 3271–3279.
(7) Sergeyev, S.; Pisula, W.; Geerts, Y. H. *Chem. Soc. Rev.* **2007**, *36*, 1902–1929.
(8) O'Neill, M.; Kelly, S. M. *Adv. Mater.* **2003**, *15*, 1135–1146.
(9) Nelson, J. *Science* **2001**, *293*, 1059–1060.
(10) Marcus, R. A. *Rev. Mod. Phys.* **1993**, *65*, 599–610.
(11) Boden, N.; Bushby, R. J.; Clements, J.; Movaghar, B.; Donovan, K. J.; Kreouzis, T. *Phys. Rev. B* **1995**, *52*, 13274–13280.
(12) Zbiri, M.; Johnson, M. R.; Haverkate, L.; Mulder, F. M.; Kearley, G. J. *Aust. J. Chem.* **2010**, *63*, 388–395.
(13) Feng, X. L.; Marcon, V.; Pisula, W.; Hansen, M. R.; Kirkpatrick, J.; Grozema, F.; Andrienko, D.; Kremer, K.; Mullen, K. *Nat. Mater.* **2009**, *8*, 421–426.
(14) Senthilkumar, K.; Grozema, F. C.; Bickelhaupt, F. M.; Siebbeles, L. D. A. *J. Chem. Phys.* **2003**, *119*, 9809–9817.
(15) Andrienko, D.; Kirkpatrick, J.; Marcon, V.; Nelson, J.; Kremer, K. *Phys. Status Solidi B* **2008**, *245*, 830–834.
(16) Van de Craats, A. M.; De Haas, M. P.; Warman, J. M. *Synth. Met.* **1997**, *86*, 2125–2126.
(17) Van de Craats, A. M.; Siebbeles, L. D. A.; Bleyl, I.; Haarer, D.; Berlin, Y. A.; Zharikov, A. A.; Warman, J. M. *J. Phys. Chem. B* **1998**, *102*, 9625–9634.
(18) Mulder, F. M.; Stride, J.; Picken, S. J.; Kouwer, P. H. J.; de Haas, M. P.; Siebbeles, L. D. A.; Kearley, G. J. *J. Am. Chem. Soc.* **2003**, *125*, 3860–3866.
(19) Kirkpatrick, J.; Marcon, V.; Nelson, J.; Kremer, K.; Andrienko, D. *Phys. Rev. Lett.* **2007**, *98*, 227402.
(20) Kirkpatrick, J.; Marcon, V.; Kremer, K.; Nelson, J.; Andrienko, D. *J. Chem. Phys.* **2008**, *129*, 094506.
(21) Kirkpatrick, J.; Marcon, V.; Kremer, K.; Nelson, J.; Andrienko, D. *Phys. Status Solidi B* **2008**, *245*, 835–838.
(22) Marcon, V.; Vehoff, T.; Kirkpatrick, J.; Jeong, C.; Yoon, D. Y.; Kremer, K.; Andrienko, D. *J. Chem. Phys.* **2008**, *129*, 094505.
(23) Andrienko, D.; Marcon, V.; Kremer, K. *J. Chem. Phys.* **2006**, *125*, 124902.
(24) Troisi, A.; Cheung, D. L.; Andrienko, D. *Phys. Rev. Lett.* **2009**, *102*, 116602.
(25) Feng, X. L.; Wu, J. S.; Ai, M.; Pisula, W.; Zhi, L. J.; Rabe, J. P.; Mullen, K. *Angew. Chem., Int. Ed.* **2007**, *46*, 3033–3036.
(26) Chandrasekhar, S.; Sadashiva, B. K.; Suresh, K. A. *Pramana* **1977**, *9*, 471–480.
(27) Shen, X.; Dong, R. Y.; Boden, N.; Bushby, R. J.; Martin, P. S.; Wood, A. *J. Chem. Phys.* **1998**, *108*, 4324–4332.
(28) Zbiri, M.; Johnson, M. R.; Kearley, G. J.; Mulder, F. M. *Theor. Chem. Acc.* **2010**, *125*, 445–451.
(29) Fontes, E.; Heiney, P. A.; Dejeu, W. H. *Phys. Rev. Lett.* **1988**, *61*, 1202–1205.
(30) Wang, T.; Yan, D. H.; Luo, J.; Zhou, E. L.; Karthaus, O.; Ringsdorf, H. *Liq. Cryst.* **1997**, *23*, 869–878.
(31) Cinacchi, G.; Colle, R.; Tani, A. *J. Phys. Chem. B* **2004**, *108*, 7969–7977.
(32) Kruglova, O.; Mencles, E.; Yildirim, Z.; Wubbenhorst, M.; Mulder, F. M.; Stride, J. A.; Picken, S. J.; Kearley, G. J. *ChemPhysChem* **2007**, *8*, 1338–1344.
(33) Kruglova, O.; Mulder, F. M.; Kotlewski, A.; Picken, S. J.; Parker, S.; Johnson, M. R.; Kearley, G. J. *Chem. Phys.* **2006**, *330*, 360–364.
(34) Yildirim, Z.; Wubbenhorst, M.; Mendes, E.; Picken, S. J.; Paraschiv, I.; Marcelis, A. T. M.; Zuilhof, H.; Sudholter, E. J. R. *J. Non-Cryst. Solids* **2005**, *351*, 2622–2628.
(35) Kneller, G. R.; Keiner, V.; Kneller, M.; Schiller, M. *Comput. Phys. Commun.* **1995**, *91*, 191–214.
(36) Hunter, C. A.; Sanders, J. K. M. *J. Am. Chem. Soc.* **1990**, *112*, 5525–5534.
(37) Jorgensen, W. L.; Severance, D. L. *J. Am. Chem. Soc.* **1990**, *112*, 4768–4774.

(38) Tsuzuki, S.; Honda, K.; Uchimaru, T.; Mikami, M.; Tanabe, K. *J. Am. Chem. Soc.* **2002**, *124*, 104–112.
(39) Sinnokrot, M. O.; Valeev, E. F.; Sherrill, C. D. *J. Am. Chem. Soc.* **2002**, *124*, 10887–10893.
(40) Lee, E. C.; Kim, D.; Jurecka, P.; Tarakeshwar, P.; Hobza, P.; Kim, K. S. *J. Phys. Chem. A* **2007**, *111*, 3446–3457.
(41) Dkhissi, A.; Ducere, J. M.; Blossey, R.; Pouchan, C. *J. Comput. Chem.* **2009**, *30*, 1179–1184.
(42) Sun, H. *J. Phys. Chem. B* **1998**, *102*, 7338–7364.
(43) McQuaid, M. J.; Sun, H.; Rigby, D. *J. Comput. Chem.* **2004**, *25*, 61–71.
(44) Rigby, D.; Sun, H.; Eichinger, B. E. *Polym. Int.* **1997**, *44*, 311–330.
(45) Berendsen, H. J. C.; Postma, J. P. M.; Vangunsteren, W. F.; Dinola, A.; Haak, J. R. *J. Chem. Phys.* **1984**, *81*, 3684–3690.
(46) Brooks, C. L.; Pettitt, B. M.; Karplus, M. *J. Chem. Phys.* **1985**, *83*, 5897–5908.
(47) McQuarrie, D. A. *Statistical Mechanics*; Harper & Row: New York, 1976.
(48) Andresen, T. L.; Krebs, F. C.; Thorup, N.; Bechgaard, K. *Chem. Mater.* **2000**, *12*, 2428–2433.